PNAS RESEARCH ARTICLE | NEUROSCIENCE

KCTD10 p.C124W variant contributes to schizophrenia by attenuating LLPS-mediated synapse formation

Chenjun Mu[a,1], Pan Liu[a,1], Liang Liu[b,1], Yaqing Wang[c,1], Kefu Liu[a], Xiangyu Li[a], Guozhong Li[a], Jianbo Cheng[a], Mengyao Bu[a], Han Chen[a], Manpei Tang[a], Yuanhang Yao[d], Jun Guan[a], Tiantian Ma[c], Zhengrong Zhou[e], Qingfeng Wu[c], Jiada Li[a,f], Hui Guo[a,f], Kun Xia[a,f], Zhengmao Hu[a,f], Xiaoqing Peng[a,f], Bing Lang[g], Faxiang Li[a,f], Xiao-wei Chen[d], Zhiheng Xu[c,2], and Ling Yuan[a,f,2]

Affiliations are included on p. 12.

Edited by Guo-li Ming, Perelman School of Medicine, University of Pennsylvania, Philadelphia, PA; received January 26, 2024; accepted October 23, 2024 by Editorial Board Member Yishi Jin

KCTD10, a member of the potassium channel tetramerization domain (KCTD) family, is implicated in neuropsychiatric disorders and functions as a substrate recognition component within the RING-type ubiquitin ligase complex. A rare de novo variant of KCTD10, p.C124W, was identified in schizophrenia cases, yet its underlying pathogenesis remains unexplored. Here, we demonstrate that heterozygous KCTD10 C124W mice display pronounced synaptic abnormalities and exhibit schizophrenia-like behaviors. Mechanistically, we reveal that KCTD10 undergoes liquid–liquid phase separation (LLPS), a process orchestrated by its intrinsically disordered region (IDR). p.C124W mutation disrupts this LLPS capability, leading to diminished degradation of RHOB and subsequent excessive accumulation in the postsynaptic density fractions. Notably, neither IDR deletion nor p.C124W mutation in KCTD10 mitigates the synaptic abnormalities caused by *Kctd10* deficiency. Thus, our findings implicate that LLPS may be associated with the pathogenesis of KCTD10-associated brain disorders and highlight the potential of targeting RHOB as a therapeutic strategy for diseases linked to mutations in KCTD10 or RHOB.

neuropsychiatric disorder | KCTD10 | liquid–liquid phase separation (LLPS) | synaptic abnormalities

Significance

Our study introduces the potential association between liquid–liquid phase separation (LLPS) disruptions and schizophrenia-like behaviors, mediated by KCTD10. We demonstrate that a de novo mutation, p.C124W, in KCTD10 compromises its LLPS capability and ability for RHOB degradation, leading to synaptic dysfunction and behavioral anomalies in heterozygous mice. This finding not only elucidates the pathogenesis of neuropsychiatric conditions but also highlights the potential of targeting Rho guanosine triphosphatase (Rho GTPase) protein, RHOB, for therapeutic intervention. The findings from our heterozygous knock-in mouse model, which is one of the few that phenocopy human schizophrenia behaviors, could pave the way for insights into the molecular mechanisms of schizophrenia and related disorders, offering a promising avenue for the development of treatments.

Liquid–liquid phase separation (LLPS) of biological macromolecules is increasingly recognized as a fundamental mechanism driving diverse biological processes. These processes include heterochromatin assembly, nucleocytoplasmic shuttling, nucleolar formation, innate immune responses, transcriptional nexus formation, stress resilience, synaptic formation and plasticity, etc (1–4).

LLPS plays a pivotal role in the formation and maintenance of neuronal synapses. Synapsin1 utilizes phase separation dynamics to orchestrate the synaptic vesicle reserve pool (5). Condensates formed by Rab3-interacting molecule (RIM) and Rab3-interacting molecule-binding protein (RIM-BP) may regulate the organization of the readily releasable pool situated proximally to the active zone (6). Moreover, the formation of postsynaptic densities relies on the assembly of multiple protein complexes through LLPS (7, 8). The phase separation dynamics of the transmembrane AMPA receptor regulatory protein/postsynaptic density 95 (TARP/PSD-95) complex also modulate synaptic transmission by concentrating α-amino-3-hydroxy-5-methyl-4-isoxazolepropionic acid receptors (AMPARs) within the postsynaptic membrane (9). Aberrant phase separation, leading to synaptic deficits or perturbed neuronal activity, is implicated in a range of human pathologies including developmental disorders such as autism (10) and Rett syndrome (11), as well as neurodegenerative diseases like amyotrophic lateral sclerosis (12, 13), multisystem proteinopathy (13, 14), Alzheimer's disease (15), and Parkinson's disease (16). However, the link between disrupted phase separation and schizophrenia has not yet been explored.

The KCTD family consists of 25 proteins, each characterized by a conserved Potassium (K^+) Channel Tetramerization Domain, a subtype of the BTB (Bric-a-brac, Tramtrack and Broad Complex) domain at the N terminus and a unique C terminus (17–19). Accumulating evidence underscores the critical roles of KCTD family genes in neurodevelopmental, neuropsychiatric, and neurodegenerative conditions (20–24). Notably, a de novo missense variant of KCTD10, p.C124W, has been identified in individuals with schizophrenia through whole exome sequencing (25). *Kctd10* null mice lead to embryonic mortality by E10.5, highlighting its essential function in embryogenesis (26). However, the specific mechanisms linking KCTD10's physiological functions to neuropsychiatric disorders including schizophrenia, remain elusive.

The authors declare no competing interest.

This article is a PNAS Direct Submission G.-l.M. is a guest editor invited by the Editorial Board.

[1]C.M., P.L., L.L., and Y.W. contributed equally to this work.

[2]To whom correspondence may be addressed. Email: zhxu@genetics.ac.cn or yuanling@sklmg.edu.cn.

This article contains supporting information online at https://www.pnas.org/lookup/suppl/doi:10.1073/pnas.2400464121/-/DCSupplemental.

Published November 20, 2024.

KCTD10 functions as a substrate recognition receptor within Really Interesting New Gene (RING)-type ubiquitin ligase complexes (27–29). Several substrates including Ras homolog family member B (RHOB), centrosomal protein 97 (CEP97), eukaryotic translation initiation factor 3D (EIF3D), T-box transcription factor 5a (TBX5a), and Toll/IL-1R domain-containing adaptor-inducing IFN-β (TRIF) are ubiquitinated and subsequently degraded by the CULLIN3 (CUL3)/KCTD10 E3 complex (30–33). RHOB has been identified as a postsynaptic element that influences synaptic plasticity and neuronal structure (34).

In this study, we found that both KCTD10 deficiency and the C124W mutation disrupt normal synaptic formation and/or maintenance. KCTD10 participates in LLPS both in vitro and in vivo. The p.C124W mutation appears to impair RHOB degradation by diminishing the LLPS capacity of KCTD10, leading to aberrant synaptic development and schizophrenia-like behaviors.

Results

***Kctd10* Deficiency Leads to Abnormal Synaptic Development and Function.** Our prior study revealed that *Kctd10* deficiency causes abnormal proliferation and differentiation of neuronal progenitors, consequently resulting in reduced brain size (35). In parallel, we conducted a quantitative mass spectrometry analysis comparing wild-type (WT) and *Kctd10*-conditional knockout (cKO) cortices, identifying 3,442 differentially expressed proteins (DEPs) (35). Gene Ontology (GO) analysis of these DEPs indicated significant enrichment in biological processes related to postsynaptic specialization, postsynaptic density, and postsynaptic membrane (*SI Appendix*, Fig. S1*A*). Consistently, synaptosome extraction from the mouse cortex revealed the presence of KCTD10 (Fig. 1*A*), and its association with the postsynaptic density (PSD) was confirmed through subcellular fractionation of mouse hippocampus (Fig. 1*B*). Furthermore, in Thy1-*GFPm* transgenic mice, costaining of KCTD10 and PSD95 demonstrated their colocalization in the hippocampal CA1 region's pyramidal neurons (Fig. 1*C*). We also generated a knock-in mouse line expressing a GFP-KCTD10 fusion protein (*SI Appendix*, Fig. S1*B*). Costaining for GFP, PSD95, and synaptophysin, a presynaptic marker, illustrated that while GFP and PSD95 signals overlapped significantly, GFP was adjacent to synaptophysin (*SI Appendix*, Fig. S1*C*), indicating that KCTD10 is primarily localized in postsynaptic regions. Further validation in cultured primary hippocampal neurons revealed robust colocalization between PSD95 and transfected mCherry-KCTD10 (*SI Appendix*, Fig. S1*D*).

To evaluate the impact of *Kctd10* deletion on synaptic development, we used Thy1-*GFPm* transgenic mice to visualize pyramidal neurons (PNs). We found a marked decrease in spine density on both apical and basal dendrites of PNs in the CA1 region of cKO hippocampus (*SI Appendix*, Fig. S2 *A–D*), affecting various spine types including mushroom, stubby, and branched spines. Additionally, the proportions of these spine types shifted, with reduced mushroom, stubby, and branched spines and increased thin and filopodia spines (*SI Appendix*, Fig. S2 *A–D*). Similar results emerged from primary cultured cKO neurons at DIV18 (*SI Appendix*, Fig. S2 *E* and *F*). Neurons transfected with *Kctd10*-targeted shRNAs (shRNA1 and shRNA4) also showed a significant reduction in spine density, especially in the Kctd10-shRNA4 group (*SI Appendix*, Fig. S2 *G* and *H*).

The impairment of synaptic structure was substantiated using transmission electron microscopy. Our analysis of PSD morphology in the hippocampal CA1 region demonstrated a significant reduction in PSD thickness in *Kctd10* cKOs (Fig. 1 *D* and *E*). Additionally, there was a notable increase in the width of the synaptic cleft in cKOs (Fig. 1 *D* and *E*). These observations underscore the essential roles of KCTD10 in the formation and/or maintenance of synapses.

KCTD10 C124W Mutation Affects Synapses Formation and/or Maintenance. To investigate the potential link between KCTD10 and psychiatric conditions, we compiled information on risk genes associated with psychiatric disorders from several sources, including PsychENCODE (36, 37), Psychiatric Genomics Consortium 3 (PGC3) (38), International Schizophrenia Consortium (ISC) (39), NPdenovo Databases (40), and Charney's work (41). We conducted enrichment analyses using these disease-related gene sets against DEPs in *Kctd10* cKO brains and potential KCTD10-interacting proteins identified via coimmunoprecipitation coupled with tandem mass spectrometry (MS/MS). A gene set associated with body mass index (BMI) from BMI genome-wide association studies (GWAS) served as a negative control (42). The analyses revealed that significant enrichment of KCTD10-interacting proteins and DEPs in proteins was only linked to schizophrenia (*SI Appendix*, Fig. S3*A*), aligning with the identification of a de novo missense variant (p.C124W) in schizophrenia patients (25).

To explore the link between the KCTD10 variant and neuropsychiatric disorders, we generated *Kctd10* C124W knock-in mice using CRISPR/Cas9-mediated site-directed mutagenesis (*SI Appendix*, Fig. S4 *A* and *B*). Significantly reduced KCTD10 levels were detected at P45 (postnatal day 45) in both the cerebral cortex and hippocampus of heterozygous ($C124W^{+/-}$) and homozygous ($C124W^{+/+}$) mice (*SI Appendix*, Fig. S4 *C* and *D*). Additionally, costaining of KCTD10 and PSD95 in the hippocampal CA1 region revealed the significantly reduced intensity of KCTD10 in both $C124W^{+/-}$ and $C124W^{+/+}$ mice (*SI Appendix*, Fig. S4*E*). Quantitative PCR analysis indicated no significant differences in *Kctd10* mRNA levels among those groups (*SI Appendix*, Fig. S4*F*). Notably, both $C124W^{+/-}$ and $C124W^{+/+}$ mice, particularly $C124W^{+/+}$ mice, exhibited increased mortality (*SI Appendix*, Fig. S4 *G* and *H*).

We employed Thy1-*GFPm* transgenic mice to examine the morphology of PN spines in hippocampal CA1 region, revealing a significant reduction in spine density on both apical and basal dendrites of both $C124W^{+/-}$ and $C124W^{+/+}$ mice (Fig. 1 *F* and *G* and *SI Appendix*, Fig. S5 *A* and *B*). Specifically, in the apical dendrites of $C124W^{+/-}$ and $C124W^{+/+}$ mice, there was a significant decrease in both the density and proportion of mushroom, stubby, and branched spines, with the exception of stubby spines where no significant difference was observed between WT and $C124W^{+/-}$ mice (Fig. 1*F* and *SI Appendix*, Fig. S5*A*). Conversely, the number and proportion of thin, long thin, and filopodium spines increased, although the count of filopodium spines did not show a significant difference (Fig. 1*F* and *SI Appendix*, Fig. S5*A*). A similar alteration in spine morphology was noted in the basal dendrites of $C124W^{+/-}$ and $C124W^{+/+}$ mice (Fig. 1*G* and *SI Appendix*, Fig. S5*B*). These findings further substantiate the involvement for KCTD10 in dendritic spine development, corroborating the results observed in *Kctd10* deficiency conditions.

***Kctd10* $C124W^{+/-}$ Mice Display Schizophrenia-Like Behaviors.** To further explore the link between the C124W variant and neuropsychiatric disorders, we conducted a series of behavioral assays on WT and *Kctd10* $C124W^{+/-}$ mice, which mimic the heterozygous mutation observed in schizophrenia patients. Prepulse inhibition (PPI) impairment, a well-recognized feature in schizophrenia patients and animal models of psychosis, served as the primary endpoint for assessing the phenotypic consequences of the mutation (43, 44). Our findings demonstrated that both 3- and 5-mo-old $C124W^{+/-}$ mice exhibited a significant reduction in PPI following prepulse stimulation compared to their WT littermates

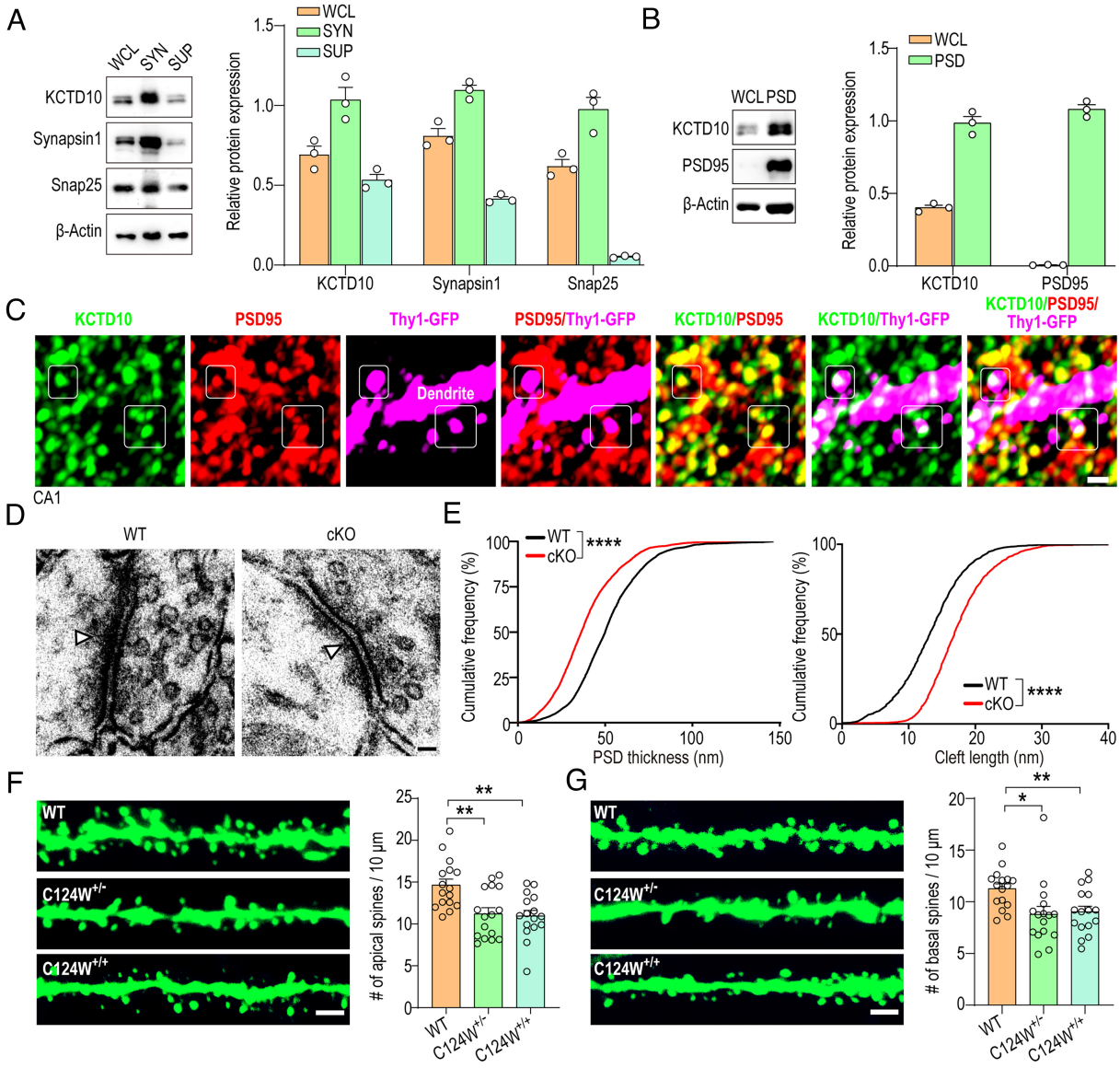

Fig. 1. *Kctd10* ablation and C124W mutation lead to abnormal synaptic formation. (*A*) Detection of KCTD10 expression in the synaptosome from the mouse cortex by western blot with Synapsin1 and Snap25. WCL, whole cell lysate; SUP, supernatant; SYN, synaptosomes. n = 3 independent experiments. (*B*) Immunoblots showing the relative levels of KCTD10 and PSD95 in subcellular fractions. PSD, postsynaptic membrane fraction. n = 3 independent experiments. (*C*) Immunofluorescence images of pyramidal neurons in hippocampal CA1 region from Thy1-GFPm mouse brain, costained with GFP (magenta), KCTD10 (green), and PSD-95 (red) antibodies. (*D*) Represented EM images of synapses from the CA1 area of the hippocampus at P21. Arrows indicate presynaptic vesicles and arrowheads represent postsynaptic densities. (*E*) Quantification of PSD thickness and cleft length in cross-sections in (*D*). WT: n = 41, cKO: n = 34 (PSD thickness), WT: n = 38, cKO: n = 27 (cleft length) sections from three animals. (*F*) *Left* panel: representative images of spines on the secondary apical dendrites of pyramidal neurons in hippocampal CA1 area of indicated mice at P30. *Right* panel: quantification of spines in the *Left* panel. WT, C124W$^{+/-}$, and C124W$^{+/+}$: n = 16/3 (n, dendrite number/brain number). (*G*) Representative images and quantification of spines on the secondary basal dendrites as in (*F*). WT, C124W$^{+/-}$, and C124W$^{+/+}$: n = 16/3 (n, dendrite number/brain number). All data are presented as means ± SEM. Student's *t* test: *P < 0.05, **P < 0.01, ****P < 0.0001. [Scale bars: 1 µm (*C*), 50 nm (*D*), 2 µm (*F* and *G*).]

(Fig. 2*A*). This decrease underscores the potential relevance of the C124W variant in modeling schizophrenia-related phenotypes.

Social withdrawal is a hallmark of neuropsychiatric disorders, including schizophrenia and autism. We first conducted a nest-building assay, which revealed a significant decrease in the nesting score of *Kctd10* C124W$^{+/-}$ mice (Fig. 2*B*). To further evaluate social interaction behaviors, particularly voluntary initiation and response to social novelty, we adopted a three-chamber social interaction test. During the sociability phase of the test, *Kctd10* C124W$^{+/-}$ mice demonstrated reduced engagement times with a novel conspecific (referred to as stranger 1 or S1), in contrast to WT littermates who displayed more frequent interactions with S1 (Fig. 2*C*). This resulted in a significantly lower social interaction preference index for the *Kctd10* C124W$^{+/-}$ mice (Fig. 2*C*). In the subsequent social novelty phase, these mice showed no preference for a newly introduced conspecific (S2), suggesting impaired social recognition (Fig. 2*C*). Additionally, the Dyadic Social Interaction test indicated a marked reduction in general sniffing and mounting behaviors among *Kctd10* C124W$^{+/-}$ mice, further underscoring the adverse effects of the C124W mutation on social behavior (Fig. 2*D*). Given the frequent observation of increased anxiety in individuals with schizophrenia, we adopted Open Field assay and found that *Kctd10* C124W$^{+/-}$ mice spent significantly less time in the center area, indicative of heightened anxiety (Fig. 2*E*). Additionally, during the light–dark Exploration test, *Kctd10* C124W$^{+/-}$ mice made fewer entries into the light box and spent less time there, further confirming their anxiety-like behavior (Fig. 2*F*). However, in

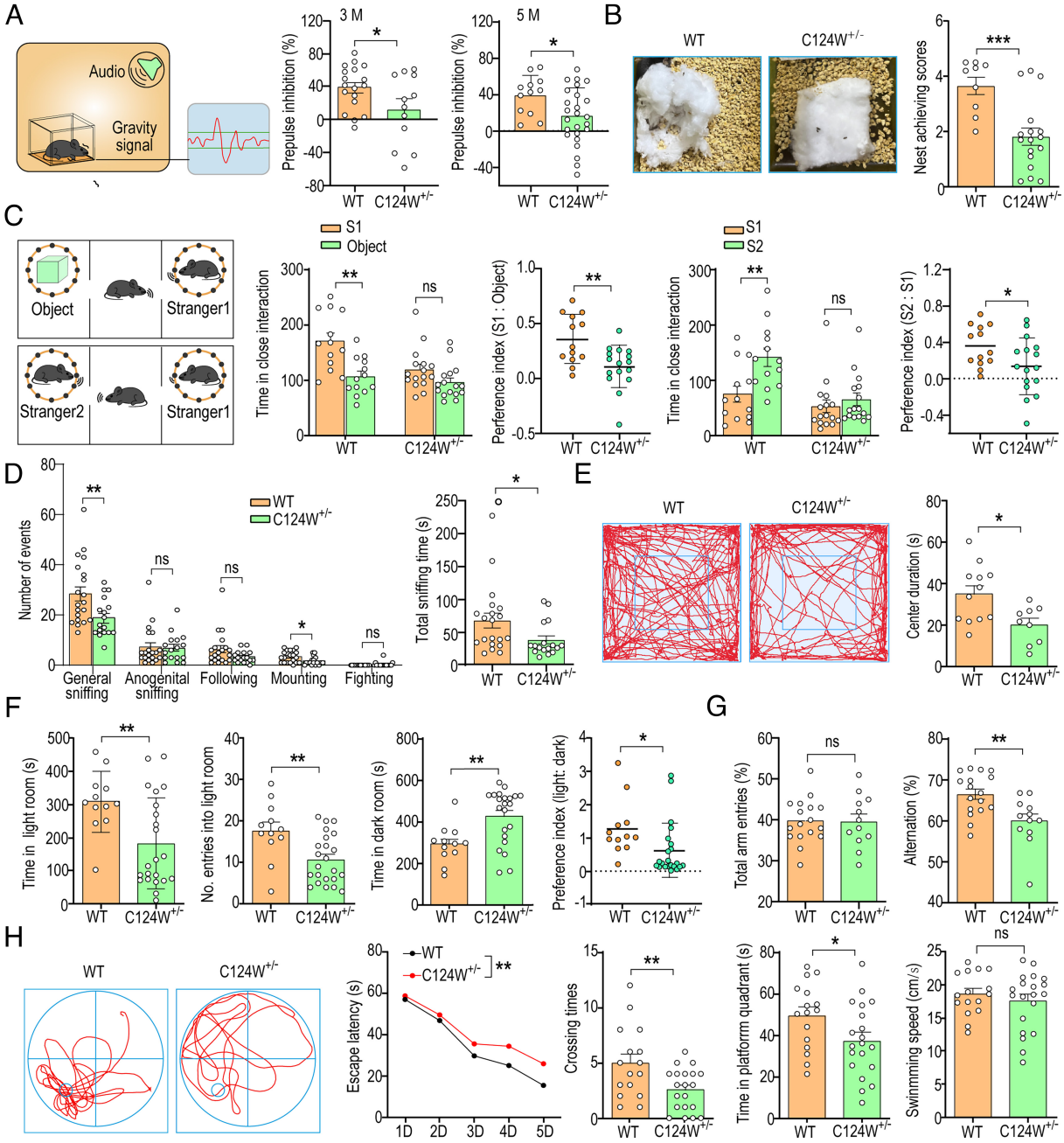

Fig. 2. C124W$^{+/-}$ mice exhibit abnormal behaviors. (*A*) Decreased PPI in C124W$^{+/-}$ mice. WT: n = 18, C124W$^{+/-}$: n = 12 (3 mo old), WT: n = 9, C124W$^{+/-}$: n = 17 (5 mo old). (*B*) *Kctd10* C124W$^{+/-}$ mice showed lower scores in the nest-building test. WT: n = 9, C124W$^{+/-}$: n = 17. (*C*) *Kctd10* C124W$^{+/-}$ mice show impaired social interaction and novelty in the 3-chamber assay. C124W$^{+/-}$ mice did not show obvious preference for the social partner (stranger 1) or novel mouse (stranger 2). WT: n = 16, C124W$^{+/-}$: n = 17. (*D*) C124W$^{+/-}$ mice exhibited a significant reduction in general sniffing and mounting events. WT: n = 20, C124W$^{+/-}$: n = 17. (*E*) Time spent in the center area analyzed in open field assay. WT: n = 12, C124W$^{+/-}$: n = 9. (*F*) Light–dark transition test. Time spent in the light and dark room, entries into the light room and preference index were examined. WT: n = 12, C124W$^{+/-}$: n = 22. (*G*) Total arm entries and effective alternation calculated in Y maze. WT: n = 17, C124W$^{+/-}$: n = 12. (*H*) C124W$^{+/-}$ mice exhibited defects in Morris water maze assay. WT: n = 15, C124W$^{+/-}$: n = 20. All data are presented as means ± SEM. *P < 0.05, **P < 0.01, ***P < 0.001. (*A*–*G*) Student's *t* test. (*H*) Two-way ANOVA and Student's *t* test.

the Elevated Plus Maze test, no significant differences were observed between the two groups (*SI Appendix*, Fig. S6*A*). Collectively, these results suggest that *Kctd10* C124W$^{+/-}$ mice demonstrate an elevated level of anxiety-related behavior.

We also assessed the learning and memory capabilities of the animals. During the Y maze test, *Kctd10* C124W$^{+/-}$ mice exhibited a significant decrease in spontaneous alternation behavior, although the total number of arm entries was comparable to that of their WT littermates (Fig. 2*G*). In the Morris Water Maze test, these mice required a significantly longer time to locate the hidden platform during the acquisition phase and spent less time in the target quadrant during the probe trial (Fig. 2*H*). No significant difference was observed in the novel object recognition test (*SI Appendix*, Fig. S6*B*). Together, these results indicate that *Kctd10* C124W$^{+/-}$ mice exhibit deficits in learning and memory. Our findings provide compelling evidence that the *Kctd10* C124W variant contributes to schizophrenia-like behaviors.

KCTD10 Undergoes Liquid–Liquid Phase Separation. To investigate the molecular mechanisms by which the KCTD10 C124W mutation influences synaptic development and induces schizophrenia-like behaviors, we transfected NIH3T3 and HeLa

cells with GFP-tagged and Flag-tagged KCTD10 constructs. Immunostaining revealed distinct punctate expression patterns in cells (Fig. 3*A* and *SI Appendix*, Fig. S7*A*). Additionally, we utilized a KCTD10 antibody for immunostaining of hippocampal CA1 pyramidal neurons labeled by Thy1-*GFPm*, and observed punctate endogenous expression of KCTD10 on dendrites and spines (*SI Appendix*, Fig. S7*B*). In live cells, we documented the coalescence of neighboring droplets, exhibiting classic droplet fusion characteristics including neck formation and relaxation into spherical shapes (Fig. 3*B*). Fission events were also noted, suggesting liquid-like properties of these structures (Fig. 3*C*). Furthermore, we examined the effects of 1,6-hexanediol, an aliphatic alcohol known to disrupt weak hydrophobic protein–protein interactions and liquid-like condensates (45, 46). Treatment with 1,6-hexanediol significantly reduced both the number and size of puncta in NIH3T3 cells (Fig. 3*D*), indicating a disruption of these protein assemblies.

To determine whether KCTD10 has the potential for in vitro phase separation, we expressed and prokaryotically purified MBP-GFP-KCTD10 fusion protein. Following purification and MBP cleavage, the purity and concentration of KCTD10 were assessed (Fig. 3*E*). In an in vitro phase separation assay utilizing the sitting-drop vapor diffusion method, robust, largely spherical KCTD10 condensates formed after 15 h of incubation. Some condensates rapidly coalesced into larger spherical droplets within seconds (Fig. 3*F*). We also employed a classical approach involving continuous protein concentration monitoring in all subsequent in vitro phase separation experiments (47). Purified GFP-KCTD10 (20 μM) was mixed with an equal volume of buffer containing 2 M NaCl and incubated at room temperature. One hour later, KCTD10 condensates formed and subsequently disintegrated upon the addition of 1,6-hexanediol (Fig. 3*G*). We quantified KCTD10 levels in hippocampal CA1 neurons using a previously established method (48), finding concentrations between 1.42 and 2.14 μM, which falls within the 0.1 to 50 μM range used in our phase separation assays (*SI Appendix*, Fig. S7*C*).

We further investigated the effects of salt concentration and KCTD10 levels on phase separation behaviors. As expected,

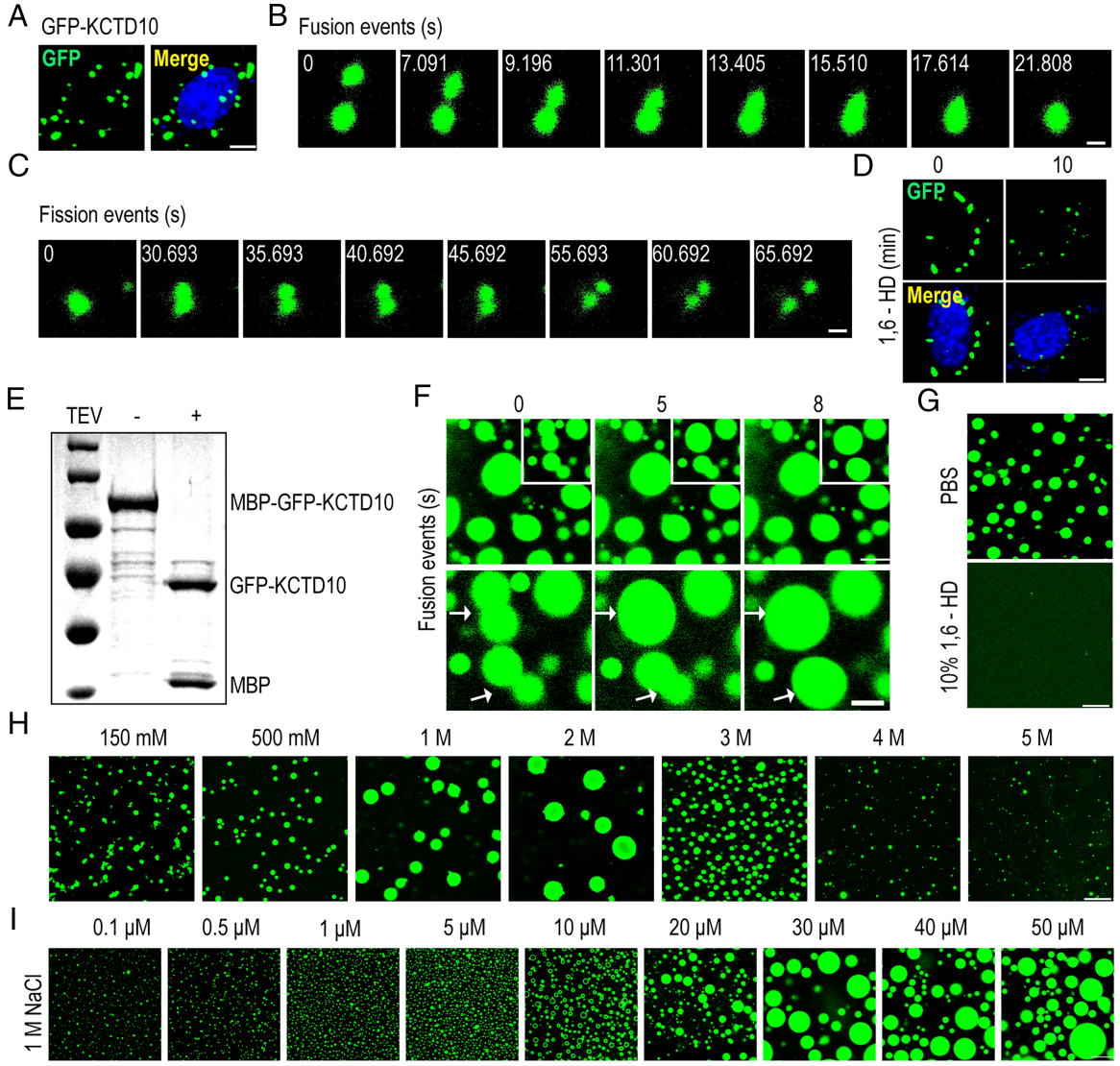

Fig. 3. KCTD10 spontaneously assembles into liquid droplets both in vivo and in vitro. (*A*) Representative images of NIH3T3 cells expressing GFP-KCTD10. (*B* and *C*) Time-lapse imaging showing droplet fusion and fission events. (*D*) Representative images of GFP-KCTD10 expressed in NIH3T3 cells with or without 10% hexanediol treatment for 10 min. (*E*) Purified recombinant KCTD10 before and after acTEV protease treatment. (*F*) Representative images showing droplet fusion event of 10 μM GFP-KCTD10 in TBS buffer (20 mM Tris, 150 mM NaCl, pH 7.6). (*G*) Representative images of droplets formed by GFP-KCTD10 in vitro before and after 10% hexanediol treatment. (*H*) Images showing phase separation ability of 10 μM of KCTD10 at various salt concentrations as indicated at 25 °C. (*I*) Fluorescence images showing the phase separation potential under different protein concentration of KCTD10 as indicated. Reaction buffer (20 mM Tris, 150 mM-5 M NaCl, pH 7.6) was used throughout this study with indicated concentration of NaCl. [Scale bars: 5 μm (*A* and *D*), 1 μm (*B* and *C*), 10 μm (*F–H*).]

increasing NaCl concentrations from 150 mM to 3 M led to rapid phase separation into numerous liquid-like droplets following 1 h of equilibration at a KCTD10 concentration of 10 μM (Fig. 3*H*). Droplets formed at 1 M and 2 M NaCl were significantly larger than those at other concentrations (Fig. 3*H*). However, these droplets disappeared when the NaCl concentration reached 4 M (Fig. 3*H*), suggesting that there is an optimal salt concentration that promotes LLPS of KCTD10. Additionally, we explored the LLPS potential of KCTD10 at varying protein concentrations (ranging from 0.1 to 50 μM) in the presence of either 1 M or 2 M NaCl. Interestingly, KCTD10 underwent phase separation at both salt concentrations across the entire protein concentration range (Fig. 3*I* and *SI Appendix*, Fig. S7*D*). Consistent with earlier observations, the phase separation of KCTD10 exhibited a concentration-dependent behavior (Fig. 3*I* and *SI Appendix*, Fig. S7*D*).

These results demonstrate that KCTD10 can autonomously form densely packed liquid droplets through LLPS and is modulated in a dose-dependent manner by both protein and salt concentrations.

Low Complexity Sequence of KCTD10 Is Essential for Liquid–Liquid Phase Separation. KCTD10 contains an intrinsically disordered region (IDR) (Fig. 4*A*), a feature known to facilitate LLPS (49–51). To investigate IDR's role in KCTD10 LLPS, we expressed both GFP-KCTD10 (KCTD10 WT) and an IDR-truncated mutant (GFP-KCTD10 ΔIDR) in NIH3T3 cells. Deletion of IDR resulted in the absence of the large, distinct puncta characteristic of GFP-KCTD10 (Fig. 4*B*).

We subsequently purified recombinant KCTD10, KCTD10 ΔIDR, and the IDR of KCTD10 (KCTD10 IDR) (Fig. 4*C*), and conducted in vitro phase separation experiments. Remarkably, the isolated IDR domain exhibited significantly enhanced LLPS proficiency compared to both KCTD10 and KCTD10 ΔIDR (Fig. 4 *D*–*G*), displaying notable droplet fusion characteristics. Conversely, removal of IDR markedly reduced the phase separation potential of KCTD10, leading to the formation of significantly smaller liquid droplets (Fig. 4 *D*–*G*). A hallmark of liquid-like condensates is their dynamic internal reorganization and rapid exchange kinetics as quantified using fluorescence recovery after photobleaching (FRAP) (48, 52). FRAP assays showed that the fluorescence in KCTD10-IDR droplets recovered efficiently within 3 min post-photobleaching (Fig. 4 *H* and *I*), more rapid than that observed in KCTD10 liquid droplets (*SI Appendix*, Fig. S10 *F* and *G*). However, deletion of IDR significantly impaired KCTD10's recovery rate (*SI Appendix*, Fig. S10 *F* and *G*).

The findings highlight the essential role of IDR in KCTD10 for LLPS. We speculated that other elements like BTB and PCNA domains could also affect phase separation. We tested this by purifying BTB and PCNA truncation mutants (KCTD10 ΔBTB, KCTD10 ΔPCNA), and a double mutant (KCTD10 ΔBTB/IDR). Unexpectedly, both KCTD10 ΔBTB and KCTD10 ΔBTB/IDR showed enhanced droplet formation compared to KCTD10 and KCTD10 ΔIDR (*SI Appendix*, Fig. S8 *A* and *B*), suggesting that BTB removal might offset IDR loss. Phase separation increased with protein concentration in both KCTD10 and KCTD10 ΔBTB, with the latter exhibiting greater phase separation (*SI Appendix*, Fig. S8 *C* and *D*). Droplets also dissolved after treatment with 1,6-hexanediol (*SI Appendix*, Fig. S8*E*), indicating a complex interaction between BTB and IDR domains in regulating KCTD10's phase separation.

Lipid Membrane Promotes the Formation of KCTD10 Condensate. High-salt conditions are known to drive the phase separation of proteins predominantly through hydrophobic and nonionic interactions, while the role of electrostatic forces is often considered negligible (53). To further elucidate the biophysical properties of KCTD10 condensates, we employed different phase separation disruptors including 1,6-hexanediol, as well as poly-uridine (PolyU) RNA and ATP, both of which are highly negatively charged molecules that disrupt phase separation through their effects on electrostatic and polar interactions (53). Only 1,6-hexanediol successfully dissolved the KCTD10 condensates under high-salt conditions (*SI Appendix*, Fig. S9*A*). This supports the hypothesis that the phase separation behavior of KCTD10 at high salt concentrations is primarily governed by hydrophobic and nonionic interactions.

The hydrophobic and nonionic interactions reminded us of the lipid bilayer, leading us to question whether synthetic membrane structure could enhance KCTD10 phase separation. As anticipated, liposomes facilitated the rapid assembly of KCTD10 condensates at physiological salt concentrations (Fig. 5*A*). However, no significant changes were observed following incubation with liposomes at high salt concentrations (Fig. 5*B*), possibly due to either liposome structure degradation or the strong assembly induced by high salt concentrations negating any additional effects. We further found that KCTD10 exhibited robust LLPS upon the addition of liposomes, independent of the ratio used (*SI Appendix*, Fig. S9*B*). Additionally, the size of the liquid droplets gradually increased with increasing protein concentrations (Fig. 5*C*). KCTD10 condensates also formed across a range of temperatures in the presence of liposomes at physiological salt concentrations. Notably, visible liquid-like droplets appeared after a 10-min incubation of KCTD10 with liposomes at 37 °C, while it took 40 min at 25 °C and 2 h at 4 °C to assemble droplets of comparable size (Fig. 5*D*). Consistently, droplets formed by both KCTD10 and KCTD10 IDR exhibited growth or merging behaviors in the presence of liposomes (Fig. 5 *E* and *F* and Movie S1). Application of 1,6-hexanediol also rapidly dispersed these assemblies (Fig. 5*G*). The removal of IDR notably reduced the size of the condensates, while the IDR of KCTD10 showed enhanced assembly formation compared to the full-length protein (Fig. 5*H*).

To further dissect the interaction between liposomes and KCTD10 condensates, we prepared large unilamellar vesicles (LUVs) with diameters ranging from 100 to 400 nm, composed of 1-palmitoyl-2-oleoyl-glycero-3-phosphocholine (POPC) and 1-hexadecanoyl-2-(9Z-octadecenoyl)-sn-glycero-3-phospho-(1′-rac-glycerol) (POPG) in a molar ratio of 9:1, supplemented with 0.2 mol% Oleoyl-2-[12-[(7-nitro-2-1,3-benzoxadiazol-4-yl) amino] dodecanoyl]-sn-Glycero-3-Phosphocholine (18:1–12:0 NBD-PC), referred to hereafter as "NBD-LUV." Upon incubation of KCTD10 with NBD-LUV, we observed that NBD-LUV coexisted within the condensates, covering the entire droplets (Fig. 5*I*). Consistent with earlier results, only 1,6-hexanediol, but not PolyU RNA or ATP, could dissolve the formed condensates (*SI Appendix*, Fig. S9*C*). These findings collectively indicate that KCTD10 and liposomes coexist within the condensate, and synthetic membranes promote the formation of larger KCTD10 condensates.

KCTD10 C124W Mutation Attenuates Its LLPS Properties. To assess the structural impact of KCTD10 C124W mutation, we utilized AlphaFold3 and observed that the structure of the KCTD10 C124W variant did not display significant alterations compared to WT KCTD10. Superimposition of the structures revealed that the side chain of C124, originally buried within a hydrophobic pocket composed of residues L98, I105, L108, L109, and L120 within the BTB domain, is replaced by a bulkier hydrophobic tryptophan in the C124W mutant. This substitution likely prompts a rearrangement of adjacent hydrophobic residues and an expansion of the hydrophobic pocket (*SI Appendix*, Fig. S10*A*). To investigate whether C124W mutation affected the LLPS capability of KCTD10, we prepared KCTD10, KCTD10

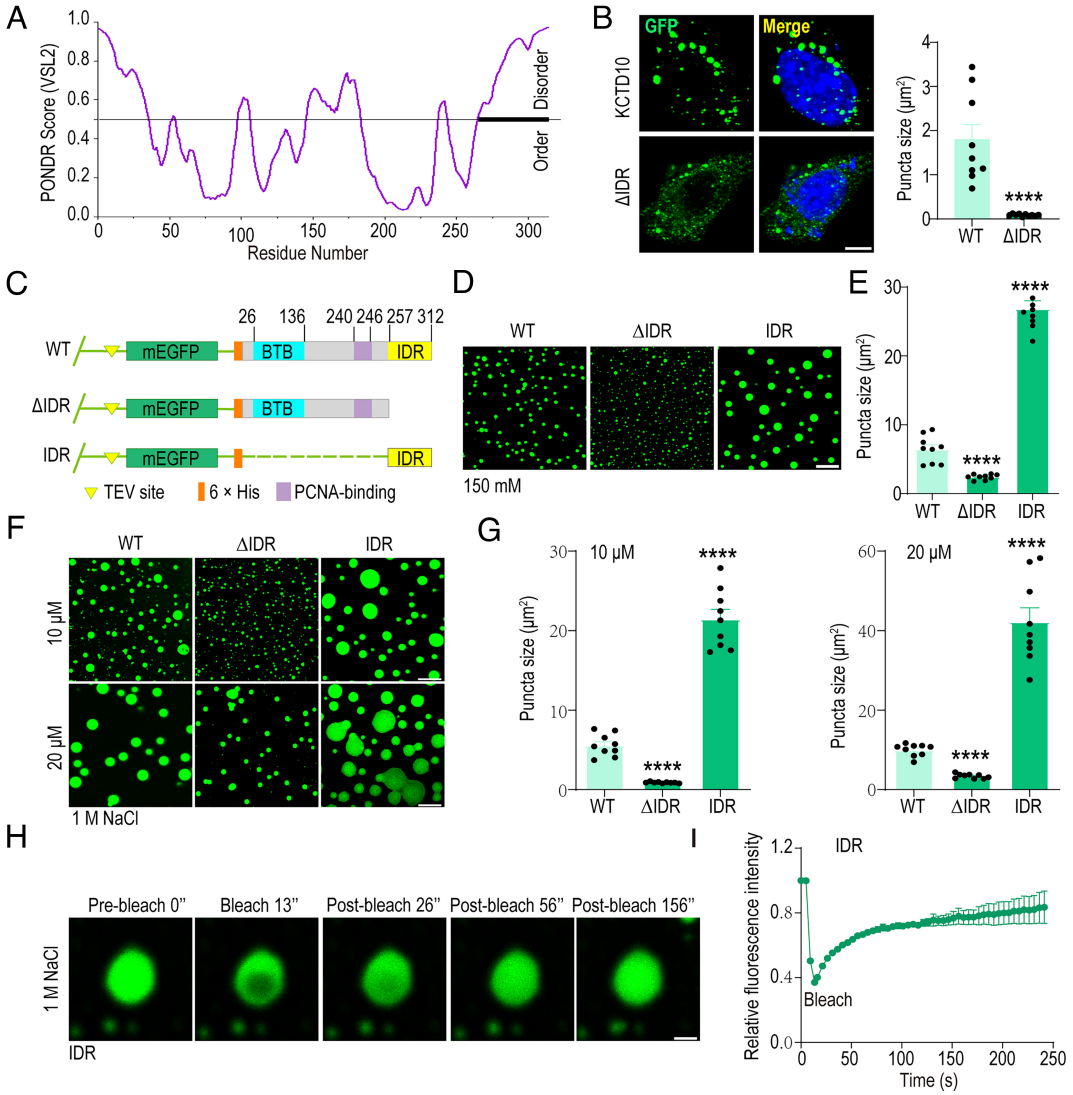

Fig. 4. KCTD10 LLPS is mediated by the C-terminal IDR sequence. (*A*) Graphs plotting intrinsic disorder (PONDR VSL2) for KCTD10. PONDR VSL2 score (*y*-axis) and amino acid position (*x*-axis) are shown. Black bar designates the IDR under investigation. (*B*) Representative images of NIH3T3 cells expressing GFP-KCTD10 and GFP-KCTD10 ΔIDR and statistical analysis for puncta size. Nuclei were stained with DAPI (blue). WT: $n = 9$, ΔIDR: $n = 10$ from >3 independent experiments. (*C*) Schematic diagram of KCTD10, KCTD10 ΔIDR, and KCTD10 IDR. (*D*) Representative images of liquid-like droplets formed by 10 μM GFP-KCTD10, GFP-KCTD10 ΔIDR, and GFP-KCTD10 IDR at 150 mM NaCl and 25 °C. (*E*) Quantification of puncta size for data in (*D*). KCTD10, KCTD10 ΔIDR, and KCTD10 IDR, $n = 9$ from >3 independent experiments. (*F*) Representative images of 10 or 20 μM KCTD10, KCTD10 ΔIDR, and KCTD10 IDR at 1 M NaCl and 25 °C. (*G*) Quantification of puncta size for data in (*F*). $n = 9$ from >3 independent experiments. (*H*) FRAP analysis of KCTD10 IDR droplets formed at 1 M NaCl with 20 μM protein at 25 °C. (*I*) Quantitative FRAP for data in (*H*). All data are presented as means ± SEM. ****$P < 0.0001$. Student's *t* test. [Scale bars: 5 μm (*B*), 10 μm (*D* and *F*), 2 μm (*H*).]

C124W, KCTD10 ΔIDR, and KCTD10 IDR. Their OD260/OD280 ratios ranged from 0.5 to 0.61, indicating no nucleic acid contamination (Fig. 6*A* and *SI Appendix*, Fig. S10 *B* and *C*). Initial turbidity assessments (optical density at 600 nm, OD600) indicated that under 1 M NaCl conditions, WT KCTD10 at 5 or 10 μM concentrations exhibited more robust droplet formation compared to the C124W and ΔIDR mutants (Fig. 6*B*). Notably, KCTD10 IDR displayed the highest droplet formation capability among those variants tested (Fig. 6*B*). Further in vitro phase separation experiments showed that both KCTD10 C124W and KCTD10 ΔIDR exhibited significantly reduced droplet formation capabilities across various concentrations including 10 and 20 μM, in the presence of 1 M NaCl at 25 °C (Fig. 6 *C* and *D*). At lower temperatures (4 °C), the KCTD10 C124W mutation resulted in smaller droplet sizes, akin to the KCTD10 ΔIDR phenotype (*SI Appendix*, Fig. S10 *D* and *E*). Additionally, under milder salt conditions (150 mM NaCl), both in the presence or absence of liposomes, KCTD10 C124W also demonstrated diminished LLPS capabilities (Fig. 6 *E*–*H*), highlighting the mutation's disruptive effects on the protein's phase separation behavior.

Furthermore, FRAP experiments revealed that the fluorescence recovery rates for KCTD10 C124W and ΔIDR foci were significantly reduced, indicating diminished internal fluidity (*SI Appendix*, Fig. S10 *F* and *G*). Given the sensitivity of phase separation to oligomerization properties, we purified KCTD10 (aa19-131) and its C124W variant (aa19-131). Molecular sieve analysis showed that the C124W mutation did not alter the molecular weight of the protein (*SI Appendix*, Fig. S11*A*). We also constructed KCTD10 and its mutants with different tags and assessed their interactions through coimmunoprecipitation (co-IP). The results indicated that neither C124W nor KCTD10 ΔIDR mutations affected their self-interactions and the formation of KCTD10 oligomers (*SI Appendix*, Fig. S11*B*).

Collectively, these results elucidate the differential LLPS behavior of the disease-associated KCTD10 variant compared to WT KCTD10, suggesting that alternations in the phase separation dynamics of KCTD10 might play a role in the pathogenesis of schizophrenia.

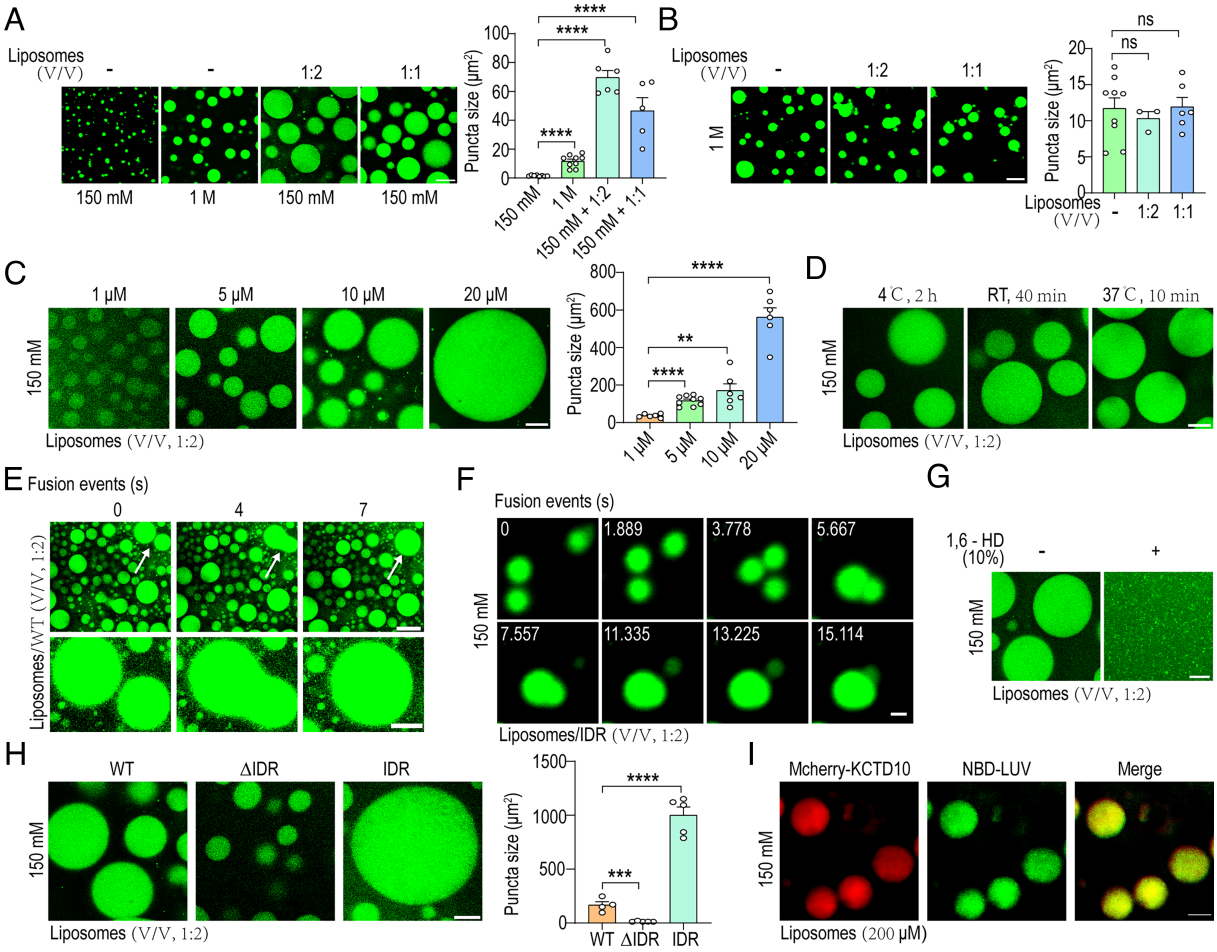

Fig. 5. Lipid membrane promotes LLPS of KCTD10. (*A* and *B*) Representative images of GFP-KCTD10 undergoing phase separation at 1 M or 150 mM NaCl mixed with different volumes of liposomes and quantification of puncta size. $n > 3$ independent experiments. (*C*) LLPS of KCTD10 enhanced with increasing protein concentration at 150 mM NaCl with the addition of liposomes. 1, 10, 20 μM: $n = 6$, 5 μM: $n = 9$ experiments from >3 biological replicates. (*D*) Representative images of GFP-KCTD10 undergoing phase separation under different temperature at 150 mM NaCl with the addition of liposomes. (*E* and *F*) The fusion phenomenon of GFP-KCTD10 and GFP-KCTD10 IDR droplets at 150 mM NaCl in the presence of liposomes. (*G*) 10% 1,6-HD disrupted the droplets formed by GFP-KCTD10 at 150 mM NaCl with the addition of liposomes. (*H*) Representative images of droplets formed by GFP-KCTD10, GFP-KCTD10 ΔIDR, and GFP-KCTD10 IDR at 150 mM NaCl with the addition of liposomes and quantification of puncta size. GFP-KCTD10 WT: $n = 8$, GFP-KCTD10 ΔIDR: $n = 9$, GFP-KCTD10 IDR: $n = 8$ experiments from >3 replicates. (*I*) Images showing the detection of liposomes (NBD-LUV) and mCherry–KCTD10 in a mixture of 200 μM liposomes and 20 μM KCTD10. LUV, large unilamellar vesicle. All data are shown as means ± SEM. $^{**}P < 0.01$, $^{***}P < 0.001$, $^{****}P < 0.0001$, ns: no significance. Student's *t* test. [Scale bars: 10 μm (*A–D* and *G–I*), 50 μm (*E*, *Top* panel), 20 μm (*E*, *Bottom* panel), 1 μm (*F*).]

KCTD10 C124W Mutation Affects Its Ability to Degrade RHOB. RHOB has been identified as a substrate for lysosomal degradation mediated by the CUL3/KCTD10 complex (28). Of note, the increased ratio of matured spines observed in RHOB knockdown neurons contrasts with the effects seen in *KCTD10* knockout or mutation models (34). This prompted us to explore the relationship between the LLPS behavior of KCTD10 and RHOB. We prepared mCherry-RHOB and mixed it in equal volumes with GFP-KCTD10 in the presence of 1 M NaCl. Both RHOB and KCTD10 underwent LLPS, forming mixed droplets (Fig. 7*A*). Furthermore, the presence of liposomes at physiological salt concentrations significantly increased the sizes of these droplets (Fig. 7*A*).

Considering the localization of KCTD10 and RHOB at postsynaptic sites, we conducted high-purity isolation of synaptosomes and PSD fractions from mouse brains to reaffirm the synaptic presence of both proteins (Fig. 7 *B* and *C* and *SI Appendix*, Fig. S12*A*). Furthermore, primary cultured neurons were cotransfected with mCherry-KCTD10 and HA-RHOB constructs. Subsequent immunostaining revealed the extensive colocalization of KCTD10, RHOB, and PSD95 at synaptic sites (*SI Appendix*, Fig. S12*B*). Next, we examined the expression of RHOB in the mouse cortex at P14 and P21. *Kctd10* deficiency led to an evident increase in RHOB levels (Fig. 7*D*). This was further confirmed in synaptosomes purified from the cortex and hippocampus, and in PSD fractions isolated from the hippocampus of mice at P21 (Fig. 7*E* and *SI Appendix*, Fig. S13 *A–D*). Elevated RHOB level was also detected in synaptosome-enriched fractions isolated from the hippocampus of $C124W^{+/+}$ mice at P60 (Fig. 7*F*). Furthermore, we cotransfected HA-RHOB and Myc-CUL3 together with Flag-KCTD10, KCTD10 ΔIDR, or KCTD10 C124W in HEK293T cells. RHOB expression was significantly reduced when coexpressed with KCTD10, but not KCTD10 ΔIDR or C124W mutants (Fig. 7*G*). Furthermore, to determine the effect of KCTD10 mutants on the ubiquitination-dependent degradation of RHOB, we transfected HA-RHOB into HEK293 cells either alone or in combination with Flag-KCTD10 WT, KCTD10 ΔIDR, or KCTD10-C124W. Both IDR deletion and C124W mutation of KCTD10 resulted in significant reductions in RHOB ubiquitination compared with WT (Fig. 7*H*). Meanwhile, co-IP results indicated that both C124W and ΔIDR mutants did not affect their interaction with CUL3 (*SI Appendix*, Fig. S14*A*). These results suggest that LLPS may play a crucial role in KCTD10-mediated ubiquitination-dependent degradation of RHOB.

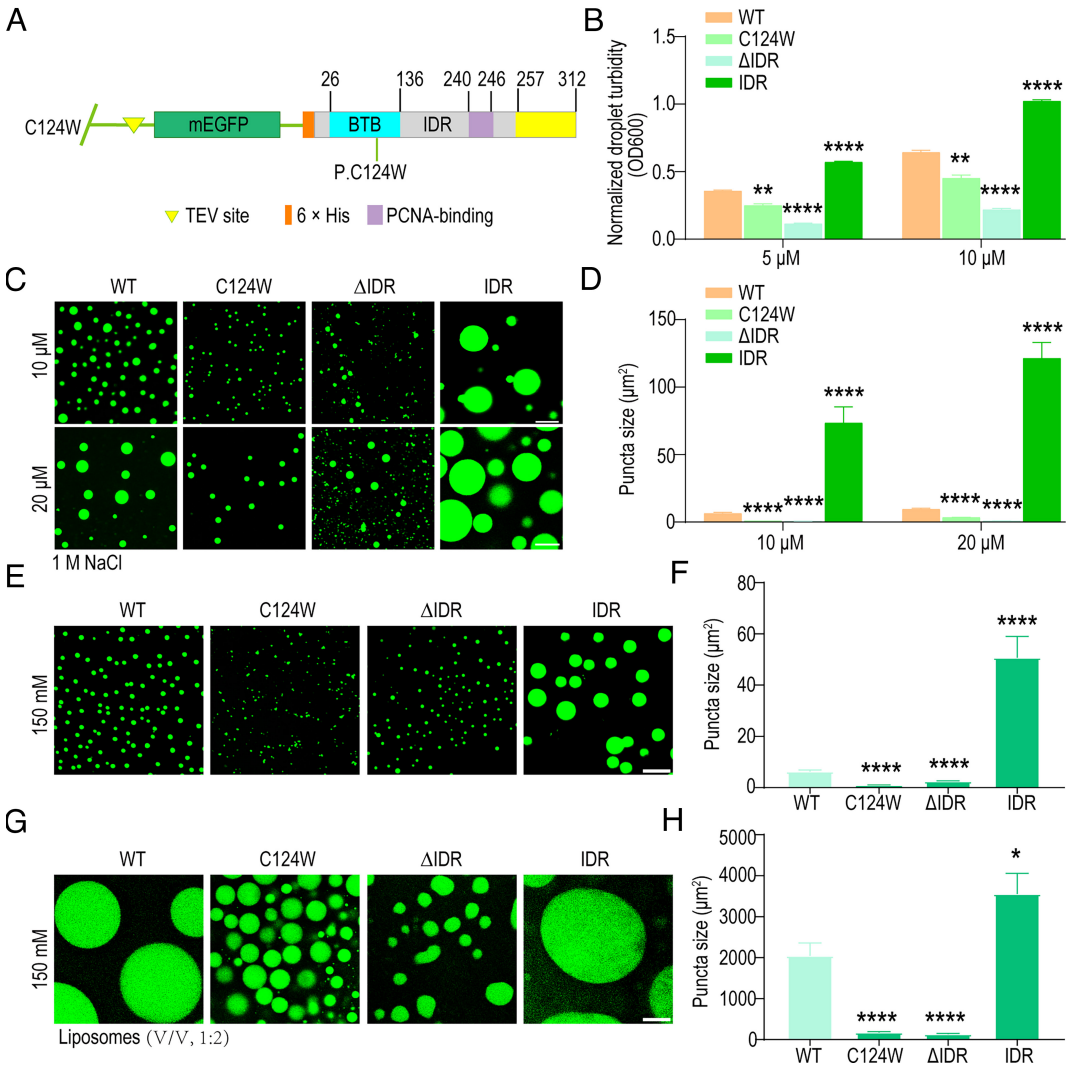

Fig. 6. Schizophrenia-associated KCTD10 variation leads to reduced LLPS capacity. (*A*) Schematic diagram of KCTD10 C124W mutation. (*B*) Quantification of solution turbidity of KCTD10 WT and indicated mutants measured at an optical density of 600 nm (OD600). *n* = 3 independent experiments. (*C*) Representative images of droplets formed by 10 or 20 μM indicated proteins at 1 M NaCl at 25 °C. (*D*) Quantification of puncta size for data in (*C*). (*E*) Representative images of condensates formed by 10 μM indicated proteins at 150 mM NaCl at 25 °C. (*F*) Quantification of puncta size for data in (*E*). (*G*) Images of condensates formed by 10 μM indicated proteins mixed with liposomes in 150 mM NaCl at 25 °C. (*H*) Quantification of puncta size for data in (*G*). All data are shown as means ± SEM. **P* < 0.05, ***P* < 0.01, *****P* < 0.0001. Student's *t* test. *n* = 9 experiments from at least 3 replicates in (*D*, *F*, and *H*). [Scale bars: 10 μm (*C*, *E*, and *G*).]

We went on to inspect the effects of KCTD10 ΔIDR and KCTD10 C124W in synaptic development. Expression of WT KCTD10 could effectively rescue the defects caused by *Kctd10* knockdown including the reduction in total spine number as well as the number and ratio of mushroom and stubby spines (Fig. 7*I* and *SI Appendix*, Fig. S15*A*). The inability of KCTD10-ΔIDR mutant to rescue these defects indicates that the IDR is essential for the function of KCTD10 in synaptic development (Fig. 7*I* and *SI Appendix*, Fig. S15*A*). It is noteworthy that C124W mutant could not rescue the reduction in the total number of spines, although it showed a slight rescue effect on the number of mushroom spines and the proportion of filopodia spines (Fig. 7*I* and *SI Appendix*, Fig. S15*A*). These observations indicate that LLPS may also play an important role in KCTD10's function in synaptic development.

Discussion

In this study, we revealed that heterozygous KCTD10 C124W mutation leads to defects in the formation and/or maintenance of dendrites and synapses and schizophrenia-like behaviors in mice. Mechanistically, KCTD10 p.C124W mutation is most likely to impair the degradation of RHOB by reducing KCTD10's ability to undergo phase separation, leading to abnormalities in synaptic development and behaviors in mice (Fig. 8).

Our identification of a number of candidate KCTD10 interacting proteins related to schizophrenia, and the reported association of KCTD10 p.C124W variant with schizophrenia promoted us to inspect the effects of KCTD10 p.C124W on mouse behaviors. We revealed that heterozygous KCTD10 p.C124W mutation resulted in significant schizophrenia-like behaviors, as well as abnormal synapse morphology in the hippocampal pyramidal neurons. This indicates that KCTD10 p.C124W mutation may result in defects in the formation and/or maintenance of synapses and subsequent abnormal behaviors.

Our study has demonstrated that KCTD10 can form condensates through LLPS. We found that environmental conditions, particularly elevated salt concentrations, significantly modulate the LLPS behavior of KCTD10. Notably, the introduction of 1,6-hexanediol effectively dissolves KCTD10 condensates under both high-salt conditions and physiological salt concentrations in the presence of liposomes. Conversely, PolyU RNA and ATP do

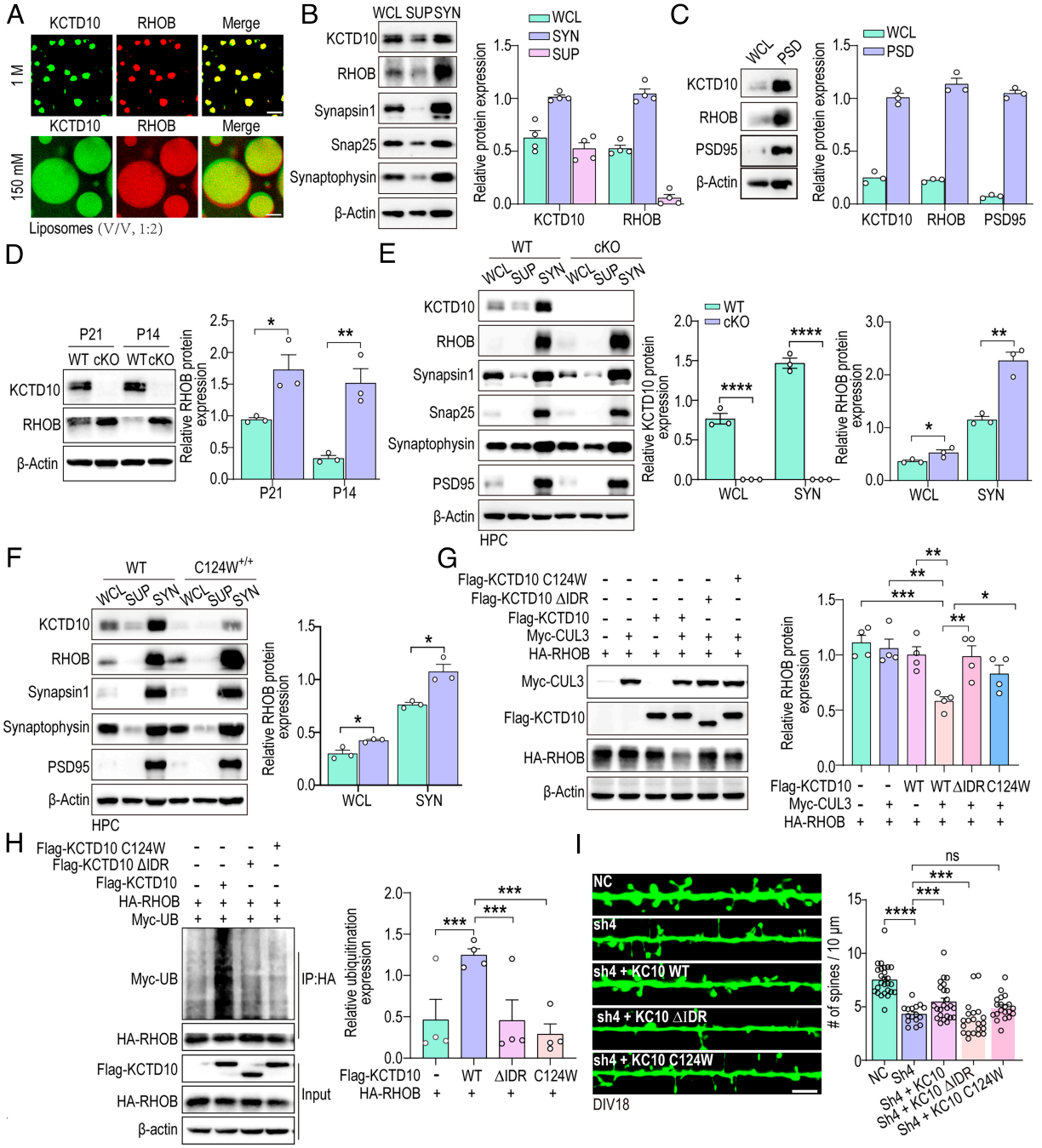

Fig. 7. Degradation of RHOB by KCTD10 requires its LLPS ability. (*A*) Confocal images of cocondensates formed by 10 μM KCTD10 (green, mGFP-KCTD10) and RHOB (red, mCherry-RHOB) in 1 M NaCl alone or 150 mM NaCl mixed with liposomes. (*B*) Levels of KCTD10 and RHOB in high purity extracted synaptosomes analyzed by western blotting with Synapsin1, Snap25, and Synaptophysin as markers for synaptosomes. $n = 4$ experiments. (*C*) Western blot analysis of KCTD10 and RHOB in the PSD fraction of the mouse hippocampus on P60. $n = 3$ experiments. (*D*) P14 and P21 cortices from *Kctd10* cKO and WT littermates were analyzed by immunoblotting for RHOB. (*E*) Synaptosome from the hippocampus of WT and *Kctd10* cKO littermates on P21 were analyzed for RHOB expression, $n = 3$ experiments. (*F*) RHOB expression in synaptosome-enriched fractions obtained from the hippocampi of WT and C124W$^{+/+}$ mice at P60, $n = 3$ experiments. (*G*) Expression of HA-RHOB, Myc-CUL3, His-UB in HEK293T cells alone or together with KCTD10 WT, KCTD10 ΔIDR, and KCTD10 C124W. Cell lysates were analyzed by immunoblotting with indicated antibodies, $n = 4$ experiments. (*H*) KCTD10, but not KCTD10 ΔIDR and KCTD10 C124W significantly induces the ubiquitination of RHOB. HA-RHOB and Myc-Ub were cotransfected with Flag-KCTD10, KCTD10 ΔIDR, or KCTD10 C124W, immunoprecipitated with HA antibody, and probed with HA, Flag, and Myc antibodies, $n = 4$ experiments. (*I*) *Left* panel: representative images of primary cultured neurons transfected with sh4 alone or together with KCTD10 WT (KC10), KC10 ΔIDR, or KC10 C124W. *Right* panel: quantification of spines in *Left* panel. $n = 16$ for each group from >3 independent experiments. All data are displayed as means ± SEM. *$P < 0.05$, **$P < 0.01$, ***$P < 0.001$, ****$P < 0.0001$, ns: no significance. Student's *t* test. [Scale bars: 10 μm (*A*), 5 μm (*I*).]

not disrupt these condensates. These observations indicate that the LLPS of KCTD10 is predominantly driven by hydrophobic and nonionic interactions. Additionally, our findings indicate that the presence of liposomes markedly accelerates the assembly of KCTD10 condensates under physiological salt conditions. Notably, these liposomes not only coexist within the condensates but also appear to envelop the entire structural assembly. This observation is underscored by the predominantly solid-circular morphology of the liposomes and a significant increase in their size. Such phenomena suggest that multiple liposomes may intermingle with the KCTD10 condensates. This intermingling could facilitate the clustering of liposomes, akin to the mechanism

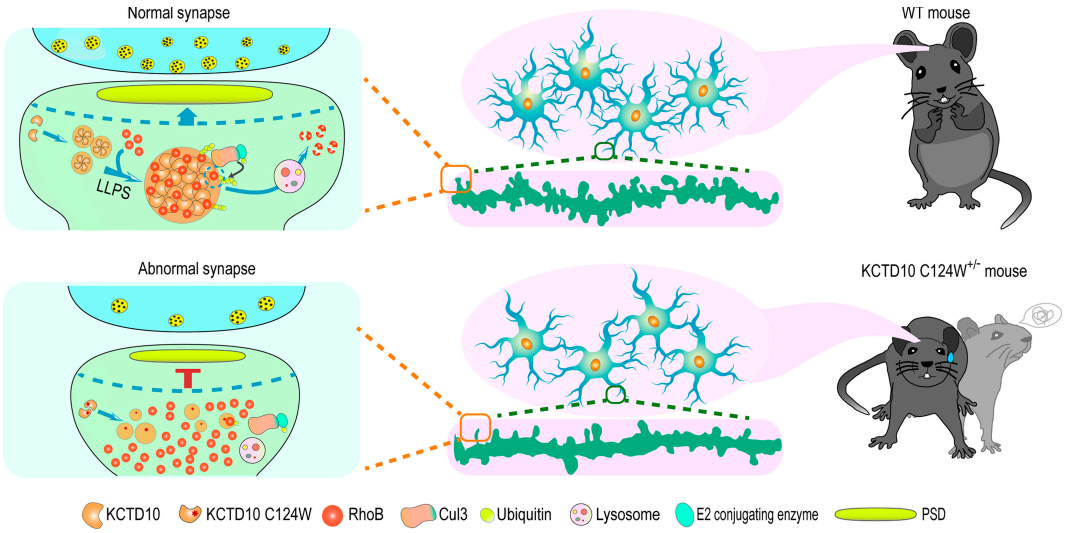

Fig. 8. Pathogenesis of KCTD10 C124W mutation. Schematic model illustrates that KCTD10 p.C124W mutation may impede the degradation of RHOB by reducing the phase separation ability of KCTD10, leading to abnormal synaptic maturation and the manifestation of schizophrenia-like behaviors in p.C124W heterozygous mice.

observed with Synapsin1 condensates, where liposome clustering is induced through interactions between protein condensates and the negatively charged phospholipids on the liposome surface (5).

LLPS is initiated either by multivalent interactions mediated by IDRs within proteins or through interactions involving protein-interacting domains (54–56). In line with previous studies, IDR of KCTD10 is essential and most likely to be responsible for mediating LLPS both in vitro and in cells, leading to the formation of punctate liquid-like structures. Unexpectedly, deletion of the BTB domain of KCTD10 significantly enhances its LLPS capacity. This indicates that different motifs in KCTD10 may precisely modulate the phase separation executed by KCTD10. The BTB domain may restrain LLPS of KCTD10 intramolecularly to ensure a balance between excessively potent or weak LLPS potential, thereby fine-tuning the phase separation ability. The location of KCTD10 p.C124W in the BTB domain that results in substantially diminished LLPS capacity suggests that the mutation leads to increased ability to inhibit the phase separation capability of KCTD10.

Moreover, we observed that the KCTD10 C124W mutation not only leads to the instability of KCTD10, but also significantly diminishes the phase separation capacity of the protein. Consequently, we hypothesize that the C124W mutation contributes to decreased ubiquitination of RHOB, resulting in its upregulation and subsequent synaptic dysfunction. This impairment likely arises partly from the direct reduction in protein levels and partly from the diminished liquid–liquid phase separation (LLPS) capability. The reduction in LLPS may further destabilize KCTD10, impairing its function in the ubiquitin–proteasome pathway. Additionally, given that the LLPS of the C124W variant is significantly reduced compared to the WT KCTD10 at equivalent concentrations, we conclude that the mutation's impact on protein stability does not directly contribute to this diminished phase separation ability.

KCTD10 is responsible for targeting multiple proteins including RHOB, for degradation through the ubiquitination-dependent pathway (28, 29, 57). RHOB plays an important role in synapse development and synaptic plasticity. Remarkably, the deficiency of KCTD10 leads to significantly elevated level of RHOB at the synaptosomes. Specifically, mutations impairing the LLPS ability of KCTD10 have a profound impact on the ubiquitination-dependent degradation of RHOB. This establishes a potentially direct link between the LLPS of KCTD10 and the degradation of RHOB. Since KCTD10 p.C124W leads to abnormal neuron morphology in synapses, contrary to RHOB deficiency, it can be postulated that KCTD10 may control the development of synapse through the regulation of RHOB stability.

More and more emerging evidence has shown that the formation of PSD, presynaptic active zone, and clustered reserve pool synaptic vesicle could be facilitated by molecular assemblies mediated through phase separation (5–8). Interestingly, we identified KCTD10 as a previously unrecognized protein highly concentrated in synaptosomes like RHOB. Mixed KCTD10 and RHOB can undergo LLPS together to form uniformly mixed liquid-like structures. Importantly, KCTD10 ΔIDR and C124W mutants cannot rescue synaptic developmental defects caused by KCTD10 deficiency. This is in support of the notion that LLPS of KCTD10 and RHOB in the synapse may be involved in the development of synapses. The potential role of cocondensates formed by KCTD10 and RHOB in regulating the assembly of synaptic structures and how they coordinate with other synaptic proteins to participate in synaptic development and signaling warrants further investigation. Furthermore, we present an update on the signaling pathway involving RHOB in synaptic development, and suggest RHOB as a potential therapeutic target for neuropsychiatric disorders associated with *KCTD10* or *RHOB* mutations.

In summary, we revealed that heterozygous mice carrying the KCTD10 C124W mutation exhibit schizophrenia-like behaviors due to defects in the formation and/or maintenance of synapses. KCTD10 p.C124W and KCTD10 ΔIDR mutations disrupt the ability of KCTD10 to undergo phase separation and subsequently impair RHOB degradation, which are likely to contribute to abnormal development of synapse and behavior in mice.

Materials and Methods

Animals. The *Kctd10*$^{fl/fl}$ mice were obtained from GemPharmatech, Nanjing, China. *Kctd10*-cKO mice were produced by breeding Kctd10fl/fl mice with Nestin-Cre mice [Jackson Laboratory, B6. Cg (SJL)-TgN (Nes-Cre)1Kln]. The Thy1-*GFPm* transgenic mice were generously provided by Yi Zuo, University of California, Santa Cruz. The KCTD10 C124W and KCTD10-GFP knock-in mice were developed by Beijing Biocytogen using CRISPR/Cas9-mediated homologous recombination.

Antibodies. The following antibodies were used for western blotting: anti-Human KCTD10 (1:1,000, PA553138, Invitrogen), anti-Flag (1:1,000, M185, MBL), anti-Human Myc (1:5,000, 9E10, Santa Cruz), anti-HA (1:5,000, M180-3, MBL), anti-RHOB (1:1,000, 2098, CST), anti-Synapsin1 (1:1,000, 106008, Synaptic Systems), anti-Snap25 (1:1,000, ab109105, Abcam), anti-Synaptophysin (1:1,000, ab32127, Abcam), anti-PSD95 (1:1,000, ZA385416, Invitrogen), and anti-β-actin (1:10,000, A5441, Sigma). The antibodies used for immunostaining were as follows: anti-Flag (1:5,000, F1804, Sigma), anti-HA (1:500, 3724, CST), anti-PSD95 (1:500, ZA385416, Invitrogen), anti-Synaptophysin (1:500, ab32594, Abcam),

anti-mCherry (1:500, OB-PGP004, Oasis Biofarm), and anti-GFP (1:1,000, ab13970, Abcam). DAPI was used for nuclear counterstaining (Invitrogen).

Statistical Analysis. Experiments were conducted at least three times to ensure accuracy. Results were presented as mean ± SEM, and analyzed using GraphPad Prism 8. Statistical comparisons between two groups were made using Student's *t* test, while one-way or two-way ANOVA with Tukey's post hoc test was used for multiple comparisons. Differences were significant at $P < 0.05$.

Other methods and materials are shown in *SI Appendix*, *Supplemental Methods and Materials*.

Data, Materials, and Software Availability. The mass spectrometry proteomics data presented in this paper are based on data previously published (35), and have been deposited in the ProteomeXchange Consortium via the PRIDE partner repository, under accession number PXD050077 (58). This study does not involve any original code. All study data are included in the article and/or supporting information.

ACKNOWLEDGMENTS. We express our gratitude to Drs. Chao Chen, Guo-li Ming, Weixiang Guo. This research was funded by the National Natural Science Foundation of China (32070980, 32271026, 81901168, 32330038, 31921002, and 32394030), the Natural Science Foundation of Hunan Province (2021JJ20075). The High Performance Computing Center of Central South University provided valuable support for this research.

Author affiliations: [a]Center for Medical Genetics, Hunan Key Laboratory of Medical Genetics, Key Lab of Rare Pediatric Diseases of Ministry of Education, School of Life Science, Central South University, Changsha, Hunan 410078, China; [b]Department of Neurology, Xuanwu Hospital, Capital Medical University, Beijing 100053, China; [c]State Key Laboratory of Molecular Developmental Biology, Institute of Genetics and Developmental Biology, Chinese Academy of Sciences, University of Chinese Academy of Sciences, Beijing 100101, China; [d]Center for Life Sciences, Institute of Molecular Medicine, School of Future Technology, Peking University, Beijing 100871, China; [e]Department of Basic Medical Sciences, Neuroscience Center, Shantou University Medical College, Shantou, Guangdong 515041, China; [f]Hunan Key Laboratory of Animal Models for Human Diseases, School of Life Science, Central South University, Changsha, Hunan 410078, China; and [g]Department of Psychiatry, The Second Xiangya Hospital of Central South University, Changsha, Hunan 410011, China

Author contributions: L.Y. designed research; C.M., P.L., L.L., Y.W., G.L., J.C., H.C., M.T., Y.Y., and J.G. performed research; K.L., X.L., M.B., Z.Z., J.L., H.G., K.X., Z.H., X.P., B.L., F.L., and X.-w.C. contributed new reagents/analytic tools; T.M., Q.W., Z.X., and L.Y. analyzed data; and Z.X. and L.Y. wrote the paper.

1. H. Zhang *et al.*, Liquid-liquid phase separation in biology: Mechanisms, physiological functions and human diseases. *Sci. China Life Sci.* **63**, 953–985 (2020).
2. G. Bai, Y. Wang, M. Zhang, Gephyrin-mediated formation of inhibitory postsynaptic density sheet via phase separation. *Cell Res.* **31**, 312–325 (2021).
3. Z. Feng, X. Chen, M. Zeng, M. Zhang, Phase separation as a mechanism for assembling dynamic postsynaptic density signalling complexes. *Curr. Opin. Neurobiol.* **57**, 1–8 (2019).
4. X. Chen, X. Wu, H. Wu, M. Zhang, Phase separation at the synapse. *Nat. Neurosci.* **23**, 301–310 (2020).
5. D. Milovanovic, Y. Wu, X. Bian, P. De Camilli, A liquid phase of synapsin and lipid vesicles. *Science* **361**, 604–607 (2018).
6. X. Wu *et al.*, RIM and RIM-BP form presynaptic active-zone-like condensates via phase separation. *Mol. Cell* **73**, 971–984.e5 (2019).
7. M. Zeng *et al.*, Phase transition in postsynaptic densities underlies formation of synaptic complexes and synaptic plasticity. *Cell* **166**, 1163–1175.e12 (2016).
8. M. Zeng *et al.*, Reconstituted postsynaptic density as a molecular platform for understanding synapse formation and plasticity. *Cell* **174**, 1172–1187.e16 (2018).
9. M. Zeng *et al.*, Phase separation-mediated TARP/MAGUK complex condensation and AMPA receptor synaptic transmission. *Neuron* **104**, 529–543.e6 (2019).
10. P. Y. Shih *et al.*, Phase separation and zinc-induced transition modulate synaptic distribution and association of autism-linked CTTNBP2 and SHANK3. *Nat. Commun.* **13**, 2664 (2022).
11. R. Tillotson *et al.*, Radically truncated MeCP2 rescues Rett syndrome-like neurological defects. *Nature* **550**, 398–401 (2017).
12. A. Patel *et al.*, A liquid-to-solid phase transition of the ALS protein FUS accelerated by disease mutation. *Cell* **162**, 1066–1077 (2015).
13. A. F. Harrison, J. Shorter, RNA-binding proteins with prion-like domains in health and disease. *Biochem. J.* **474**, 1417–1438 (2017).
14. A. Molliex *et al.*, Phase separation by low complexity domains promotes stress granule assembly and drives pathological fibrillization. *Cell* **163**, 123–133 (2015).
15. S. Wegmann *et al.*, Tau protein liquid-liquid phase separation can initiate tau aggregation. *EMBO J.* **37**, 7 (2018).
16. S. Ray *et al.*, Alpha-synuclein aggregation nucleates through liquid-liquid phase separation. *Nat. Chem.* **12**, 705–716 (2020).
17. O. Albagli, P. Dhordain, C. Deweindt, G. Lecocq, D. Leprince, The BTB/POZ domain: A new protein-protein interaction motif common to DNA- and actin-binding proteins. *Cell Growth Differ.* **6**, 1193–1198 (1995).
18. V. J. Bardwell, R. Treisman, The POZ domain: A conserved protein-protein interaction motif. *Genes Dev.* **8**, 1664–1677 (1994).
19. P. J. Stogios, G. S. Downs, J. J. Jauhal, S. K. Nandra, G. G. Prive, Sequence and structural analysis of BTB domain proteins. *Genome Biol.* **6**, R82 (2005).
20. A. M. Alazami *et al.*, Accelerating novel candidate gene discovery in neurogenetic disorders via whole-exome sequencing of prescreened multiplex consanguineous families. *Cell Rep.* **10**, 148–161 (2015).
21. D. Trujillano *et al.*, Clinical exome sequencing: Results from 2819 samples reflecting 1000 families. *Eur. J. Hum. Genet.* **25**, 176–182 (2017).
22. C. Golzio *et al.*, KCTD13 is a major driver of mirrored neuroanatomical phenotypes of the 16p11.2 copy number variant. *Nature* **485**, 363–367 (2012).
23. I. Iossifov *et al.*, The contribution of de novo coding mutations to autism spectrum disorder. *Nature* **515**, 216–221 (2014).
24. S. De Rubeis *et al.*, Synaptic, transcriptional and chromatin genes disrupted in autism. *Nature* **515**, 209–215 (2014).
25. D. P. Howrigan *et al.*, Exome sequencing in schizophrenia-affected parent–offspring trios reveals risk conferred by protein-coding de novo mutations. *Nat. Neurosci.* **23**, 185–193 (2020).
26. K. Ren *et al.*, KCTD10 is involved in the cardiovascular system and Notch signaling during early embryonic development. *PLoS One* **9**, e112275 (2014).
27. F. Rodriguez-Perez *et al.*, Ubiquitin-dependent remodeling of the actin cytoskeleton drives cell fusion. *Dev. Cell* **56**, 588–601.e9 (2021).
28. I. Kovacevic *et al.*, The Cullin-3-Rbx1-KCTD10 complex controls endothelial barrier function via K63 ubiquitination of RhoB. *J. Cell Biol.* **217**, 1015–1032 (2018).
29. X. Tong *et al.*, Kctd10 regulates heart morphogenesis by repressing the transcriptional activity of Tbx5a in zebrafish. *Nat. Commun.* **5**, 3153 (2014).
30. A. Murakami *et al.*, Cullin-3/KCTD10 E3 complex is essential for Rac1 activation through RhoB degradation in human epidermal growth factor receptor 2-positive breast cancer cells. *Cancer Sci.* **110**, 650–661 (2019).
31. T. Nagai, S. Mukoyama, H. Kagiwada, N. Goshima, K. Mizuno, Cullin-3-KCTD10-mediated CEP97 degradation promotes primary cilium formation. *J. Cell Sci.* **131**, jcs219527 (2018).
32. M. Maekawa *et al.*, Cullin-3/KCTD10 complex is essential for K27-polyubiquitination of EIF3D in human hepatocellular carcinoma HepG2 cells. *Biochem. Biophys. Res. Commun.* **516**, 1116–1122 (2019).
33. X. Wu *et al.*, Regulation of TRIF-mediated innate immune response by K27-linked polyubiquitination and deubiquitination. *Nat. Commun.* **10**, 4115 (2019).
34. K. McNair *et al.*, A role for RhoB in synaptic plasticity and the regulation of neuronal morphology. *J. Neurosci.* **30**, 3508–3517 (2010).
35. J. Cheng *et al.*, KCTD10 regulates brain development by destabilizing brain disorder-associated protein KCTD13. *Proc. Natl. Acad. Sci. U.S.A.* **121**, e2315707121 (2024).
36. M. J. Gandal *et al.*, Shared molecular neuropathology across major psychiatric disorders parallels polygenic overlap. *Science* **359**, 693–697 (2018).
37. M. J. Gandal *et al.*, Transcriptome-wide isoform-level dysregulation in ASD, schizophrenia, and bipolar disorder. *Science* **362**, eaat8127 (2018).
38. V. Trubetskoy *et al.*, Mapping genomic loci implicates genes and synaptic biology in schizophrenia. *Nature* **604**, 502–508 (2022).
39. M. Ayalew *et al.*, Convergent functional genomics of schizophrenia: From comprehensive understanding to genetic risk prediction. *Mol. Psychiatry* **17**, 887–905 (2012).
40. J. Li *et al.*, Genes with de novo mutations are shared by four neuropsychiatric disorders discovered from NPdenovo database. *Mol Psychiatry* **21**, 290–297 (2016).
41. A. W. Charney *et al.*, Contribution of rare copy number variants to bipolar disorder risk is limited to schizoaffective cases. *Biol. Psychiatry* **86**, 110–119 (2019).
42. A. E. Locke *et al.*, Genetic studies of body mass index yield new insights for obesity biology. *Nature* **518**, 197–206 (2015).
43. M. A. Geyer, B. Ellenbroek, Animal behavior models of the mechanisms underlying antipsychotic atypicality. *Prog. Neuropsychopharmacol. Biol. Psychiatry* **27**, 1071–1079 (2003).
44. M. A. Geyer, K. Krebs-Thomson, D. L. Braff, N. R. Swerdlow, Pharmacological studies of prepulse inhibition models of sensorimotor gating deficits in schizophrenia: A decade in review. *Psychopharmacology (Berl.)* **156**, 117–154 (2001).
45. S. Kroschwald, S. Maharana, A. Simon, Hexanediol: A chemical probe to investigate the material properties of membrane-less compartments. *Matters* **3**, e201702000010 (2017).
46. B. R. Sabari *et al.*, Coactivator condensation at super-enhancers links phase separation and gene control. *Science* **361**, eaar3958 (2018).
47. S. Alberti, A. Gladfelter, T. Mittag, Considerations and challenges in studying liquid-liquid phase separation and biomolecular condensates. *Cell* **176**, 419–434 (2019).
48. Y. Shin, C. P. Brangwynne, Liquid phase condensation in cell physiology and disease. *Science* **357**, 6357 (2017).
49. R. Ravindran *et al.*, Peroxisome biogenesis initiated by protein phase separation. *Nature* **617**, 608–615 (2023).
50. A. Patil *et al.*, A disordered region controls cBAF activity via condensation and partner recruitment. *Cell* **186**, 4936–4955.e26 (2023).
51. J. Y. Kang *et al.*, LLPS of FXR1 drives spermiogenesis by activating translation of stored mRNAs. *Science* **377**, eabj6647 (2022).
52. S. F. Banani, H. O. Lee, A. A. Hyman, M. K. Rosen, Biomolecular condensates: Organizers of cellular biochemistry. *Nat. Rev. Mol. Cell Biol.* **18**, 285–298 (2017).
53. G. Krainer *et al.*, Reentrant liquid condensate phase of proteins is stabilized by hydrophobic and non-ionic interactions. *Nat. Commun.* **12**, 1085 (2021).
54. J. H. Ahn *et al.*, Phase separation drives aberrant chromatin looping and cancer development. *Nature* **595**, 591–595 (2021).
55. Y. Shin *et al.*, Spatiotemporal control of intracellular phase transitions using light-activated optoDroplets. *Cell* **168**, 159–171.e14 (2017).
56. R. Ahmed, J. D. Forman-Kay, Aberrant phase separation: Linking IDR mutations to disease. *Cell Res.* **33**, 583–584 (2023).
57. M. S. Ye *et al.*, KCTD10 regulates brown adipose tissue thermogenesis and metabolic function via Notch signaling. *J. Endocrinol.* **252**, 155–166 (2022).
58. Y. Perez-Riverol *et al.*, The PRIDE database resources in 2022: A hub for mass spectrometry-based proteomics evidences. *Nucleic Acids Res.* **50**, D543–D552 (2022).